Oxidation of two-dimensional electrides: Structural transition and the formation of half-metallic channels protected by oxide layers

Pedro H. Souza,[1,*] Danilo Kuritza,[2,†] José E. Padilha,[2,‡] and Roberto H. Miwa[1,§]
[1]*Instituto de Física, Universidade Federal de Uberlândia, C.P. 593, 38400-902, Uberlândia, MG, Brazil*
[2]*Campus Avançado Jandaia do Sul, Universidade Federal do Paraná, 86900-000, Jandaia do Sul, PR, Brazil*

(Received 25 February 2022; revised 25 April 2022; accepted 24 May 2022; published 2 June 2022)

Based on first-principles calculations, we performed a systematic study of the energetic stability, structural characterization, and electronic properties of the fully oxidized A_2B electrenes, with the following combinations: (i) A = Ca, Sr, and Ba for B = N; (ii) A = Sr and Ba for B = P; and Y_2C and Ba_2As. We have considered one side oxidation of single layer electrenes (O/A_2B), and two side oxidation of bilayer electrenes (O/$(A_2B)_2$/O). We show that the hexagonal lattice of the pristine host is no longer the ground state structure in the (fully) oxidized systems. Our total energy results reveal an exothermic structural transition from hexagonal to tetragonal (h→t) geometry, resulting in layered tetragonal structures [$(AOAB)^t$ and $(AO(AB)_2AO)^t$]. Phonon spectra calculations and molecular dynamic simulations show that the O/A_2B and O/$(A_2B)_2$/O systems, with A = Ba, Ca, Sr, and B = N, become dynamically and structurally stable upon such a h→t transition. Further structural characterizations were performed based on simulations of the near edge x-ray absorption spectroscopy at the nitrogen K edge. Finally, the electronic band structure and transport calculations reveal the formation of half-metallic bands spreading out through the AN layers, which in turn are shielded by oxide AO sheets. These findings indicate that $(AOAN)^t$ and $(AO(AN)_2AO)^t$ are quite interesting platforms for application in spintronics; since the half-metallic channels along the AN or $(AN)_2$ layers (core) are protected against the environment conditions by the oxidized AO sheets (cover shells).

DOI: 10.1103/PhysRevB.105.235301

I. INTRODUCTION

Research works in two-dimensional (2D) materials with different functionalities have been boosted in the last few years. Since the successful synthesis of graphene [1], 2D materials have been considered as a new paradigm not only in fundamental studies, like the search of topological phases [2–4] and tunable magnetic structures in 2D systems [5–8], but also addressing technological applications. For instance, the development of new materials for (nano)electronic and spintronic devices like single layer field effect transistors [9], and half-metals based on transition metal dichalcogenides and dihalides [10–14].

Electrides are ionic crystals characterized by the presence of electrons not bonded to a particular nucleus. These electrons act as ions (with no nucleus) embedded within the crystal lattice, termed anionic electrons [15,16]. Further experimental works on Ca_2N crystals revealed that these anionic electrons form a nearly free electron gas (NFEG) confined between the stacked layers of the electride [17,18]. It is worth noting that there are other native inorganic electrides with the same lattice structure of Ca_2N, like Sr_2N [19] and Y_2C [20]; meanwhile other ones that also share the same lattice structure of Ca_2N have been predicted throughout high-throughput computational simulations, for instance, Ba_2N, Sr_2P, Ba_2P, Y_2C, and Ba_2As [21–24].

By taking advantage of the layered structure of their three-dimensional (3D) parents, combined with a suitable balance between strong (weak) intralayer (interlayer) binding interactions [25], two-dimensional materials can be obtained through exfoliation processes. Indeed, in a seminal work, Lee *et al.* [17] revealed the exfoliable nature, and the two-dimensional electronic confinement in Ca_2N electrides. Meanwhile, theoretical works based on first-principles calculations have studied the exfoliable nature of Ca_2N, as well as the electronic properties and energetic/structural stability of Ca_2N electrenes [26–28].

Currently, few layer systems of electrides (electrenes) have attracted research works in fundamental issues, like the search of topological phases throughout the design of kagome lattices on the electrene surface [29], as well as to the development of electronic devices with hight carrier density and electronic mobility. Furthermore, theoretical studies have addressed the functionalization of Ca_2N electrenes mediated by atomic adsorption [30]. Functionalization is a quite promising route in order to tailor the electronic and magnetic properties of 2D systems. For instance, the rise of ferromagnetic (FM) phases upon full hydrogenation [31], and oxidation of Ca_2N and Sr_2N electrenes [32,33]. On the other hand, it is important to stress that the presence of anionic electrons makes the electrene surface very reactive, which may lead to significant changes on the electronic and structural properties of the

*psouza8628@gmail.com
†danilo.kuritza@gmail.com
‡jose.padilha@ufpr.br
§hiroki@ufu.br

functionalized systems, giving rise to a new set of physical properties to be exploited.

In this work, by means of first-principles calculations, we perform a systematic investigation of the energetic stability, structural, and the electronic/magnetic properties of the oxidized A_2B electrenes, with the following combinations, (i) A = Ca, Sr, and Ba for B = N; (ii) A = Sr and Ba for B = P; and Y_2C and Ba_2As. We have considered the full oxidation of one surface side of single layer electrene (O/A_2B), and two surface sides in bilayer electrenes (O/$(A_2B)_2$/O). Our total energy results revealed a barrierless hexagonal (h) to tetragonal (t) structural transition, giving rise to layered tetragonal systems, namely $(AOAB)^t$ and $(AO(AB)_2AO)^t$. The dynamical and structural stabilities were examined through a combination of phonon spectra calculations, and molecular dynamic simulations. Based on the simulations of the (N K edge) x-ray absorption near edge spectroscopy (XANES), and the projection of the electronic orbitals, we present a detailed structural analysis of the oxidized systems, and fingerprints of their tetragonal geometries. Finally, focusing on the electronic/magnetic properties, we find that the oxidized $(AOAB)^t$ and $(AO(AB)_2AO)^t$ systems are characterized by (i) an energetic preference for the FM phase, and (ii) the emergence of half-metallic channels along AN layers shielded by oxidized AO shells (with A = Ca, Sr, and Ba).

II. COMPUTATIONAL DETAILS

The calculations were performed by using the density functional theory (DFT) [34] as implemented in the computational codes QUANTUM ESPRESSO (QE) [35] and Vienna *ab initio* simulation package (VASP) [36,37]. We have considered the generalized gradient approximation of Perdew-Burke-Ernzerhof (GGA-PBE) [38] for the exchange-correlation functional, and the electron-ion interactions were described using norm-conserving pseudopotentials (PS) [39] and projected augmented wave (PAW) [40] in the QE and VASP codes, respectively. The single layer and bilayer A_2B electrenes were simulated using slab structures within the supercell approach, with a vacuum region of 18 and 22 Å, respectively, and surface periodicities of (1×1), and $(\sqrt{2} \times \sqrt{2})$ for hexagonal and tetragonal structures. Dipole corrections have been included in order to suppress artificial electric fields (in asymmetric systems) across the slab [41]. The final atomic geometries, and total energies, were obtained using the QE code, where the Kohn-Sham [42] orbitals, and the self-consistent total charge densities, were expanded in plane wave basis sets with energy cutoffs of 70 and 353 Ry; the Brillouin zone sampling was performed by using a $8 \times 8 \times 1$ k-point mesh [43,44]. The atomic positions were relaxed until the residual forces were converged to within 5 meV/Å, and the structural relaxation (variable cell) was performed within a pressure convergence of 0.05 kbar. The long-range van der Waals (vdW) interactions were taken into account using the self-consistent vdW-DF approach [45–47].

Further structural characterizations were performed through calculations of the x-ray absorption spectra combining the QE results and Xspectra [48–50] simulations. We have considered the K-edge spectra of nitrogen atoms by using the gauge-including projector augmented-wave (GIPAW) [51] method to calculate the dipolar cross section,

$$\sigma(\omega) \propto \sum_n |\langle \psi_n | \hat{\varepsilon} \cdot \mathbf{r} | \psi_{1s} \rangle|^2 \delta(\epsilon_n - \epsilon_{1s} - \hbar\omega),$$

within the dipole approximation; ψ_n/ϵ_n and ψ_{1s}/ϵ_{1s} are the final n and initial $1s$ (single particle) orbitals/energies in the presence of core-hole. The absorbing atom is described with a pseudopotential with a full core-hole in the N-$1s$ orbital [52]. In order eliminate spurious interactions between a core-hole and its periodic images, we have considered a distance of ∼7 Å between the core-holes.

The electronic structure calculations and structural/thermal stability simulations were performed using the VASP code. We have considered an energy cutoff of 500 eV for the plane wave basis set, and the Brillouin zone was sampled using a $15 \times 15 \times 1$ k-point mesh [43]. The structural stability was verified through the calculation of elastic constants and the phonon dispersion using PHONOPY code [53]. The thermal stability was verified by *ab initio* molecular dynamics simulations (AIMD) at 300 K, with a time step of 1 fs using Nosé heat bath scheme [54].

The calculation of the electronic transmission probability (T) was performed based on the nonequilibrium Green's functions (NEGF) formalism using the DFT Hamiltonian as implemented in the Siesta and TranSiesta [55,56] codes. The KS orbitals were expanded in a linear combination of numerical pseudoatomic orbitals, using split-valence double-zeta basis set including polarization functions [57,58]. The BZ samplings were performed using two different sets of k-point meshes, $1 \times 10 \times 200$ $1 \times 20 \times 500$ according to the electronic transport directions.

The total transmission probability of electrons with energy E and bias voltage V, $T(E, V)$, from the left electrode to reach the right electrode passing through the scattering region is given by

$$T(E) = \mathrm{Tr}[\Gamma_R(E, V) G^R(E, V) \Gamma_L(E, V) G^A(E, V)],$$

where $\Gamma_{L,(R)}(E, V)$ is the coupling with the left and right electrodes and $G^{R,(A)}$ is the retarded (advanced) Green function matrix of the scattering region. The current I is evaluated by using Landauer-Büttiker formula [59,60],

$$I(V) = \frac{2e}{h} \int T(E, V)[f(E - \mu_L) - f(E - \mu_R)]dE,$$

where $f(\epsilon)$ is the Fermi-Dirac distribution for energy ϵ and $\mu_{L(R)}$ is the electrochemical potential of the left (right) electrode. We have considered the zero-bias approximation $T(E, V) \approx T(E, 0)$ for the calculation of the electronic current at the limit of low bias voltage ($\leqslant$0.1 V).

III. RESULTS AND DISCUSSIONS

A. Pristine A_2B electrenes

The A_2B electrides with A = Ca, Sr, Ba, Y, and B = N, P, As, C share the same structure of Ca_2N, Fig. 1(a). Our results of equilibrium geometries of A_2B electrides and 2D single layer electrenes, summarized in Table I, are in good agreement with previous experimental and theoretical findings, viz. Ba_2As [61], Ba_2P [61], Sr_2P [61], Y_2C [20,62], Ca_2N [31,32,63,64], Sr_2N [19,32], and Ba_2N [32,65]. The

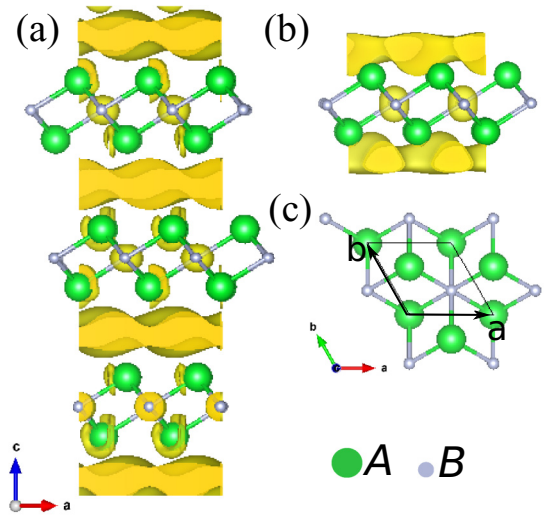

FIG. 1. Structural model of A_2B electride bulk (a), and single layer electrene, side view (b) and top view (c). The isosurfaces (of $0.003e/\text{Å}^3$) show the localization of the anionic electrons within the energy interval of ± 0.5 eV with respect to the Fermi level.

structural properties of these electrides are anisotropic, characterized by a strong intralayer interaction due to the A–B ionic chemical bonds, and a comparatively weaker interlayer interaction between the A_2B sheets. The latter is ruled by a superposition of (i) Coulombic attractive forces between the positively charged A_2B layer and the anionic electrons, and (ii) repulsive interaction between the positively charged A_2B layers [15,26,27]. In order to provide a quantitative picture of the interlayer binding strength, we calculate the interlayer binding energy (E^b) defined as [66]

$$E^b = \frac{1}{S}(E[A_2B]_{\text{ML}} - E[A_2B]_{\text{Bulk}}),$$

where $E[A_2B]_{\text{ML}}$ and $E[A_2B]_{\text{Bulk}}$ are the total energies of single layer electrene and A_2B electride, respectively, and S is the surface area normal to the A_2B stacking. Our results of binding energies for Ca_2N, Sr_2N, Ba_2N, and Y_2C (Table I) are in good agreement with those presented in the current literature [16,67].

TABLE I. Details of the equilibrium geometry of A_2B electrides and single layer electrenes, lattice constant a, and A–B equilibrium bond length (in Å), and the interlayer binding energy E^b (in J/m^2) without/with the inclusion of vdW interactions.

	Bulk			Monolayer	
A_2B	a	A–B	E^b	a	A–B
Ba_2As	4.64	3.21	0.41/0.48	4.65	3.22
Ba_2P	4.65	3.18	0.44/0.51	4.64	3.17
Sr_2P	4.45	3.01	0.59/0.64	4.43	3.00
Y_2C	3.61	2.47	1.60/1.73	3.50	2.45
Ca_2N	3.60	2.42	0.97/1.02	3.61	2.43
Sr_2N	3.84	2.60	0.78/0.83	3.85	2.61
Ba_2N	4.02	2.76	0.58/0.64	4.00	2.75

Given the large A_2B–A_2B interlayer distance (>3 Å), it is worth examining the contribution of the van der Waals (vdW) interactions in the binding energies. As shown in Table I, the calculations of E^b without/with the inclusion of the vdW interactions reveal a slight increase of E^b, for instance between 5% and 10% for the nitrides A_2N. Thus, we can infer that the Coulombic attractive forces bring the major contribution to the interlayer interactions.

Our results of E^b indicate that these A_2B electrenes can be classified as "potentially exfoliable" based on the criteria presented by Mounet *et al.*, in a recent high-throughput computational investigation applied to two-dimensional material [25]. As shown in Figs. 1(b) and 1(c), at the equilibrium geometry, the single layer electrene exhibits the same A_2B atomic structure of its bulk (electride) parent, with the anionic electrons lying on the electrene surface.

B. Oxidation

Here we will address the energetic stability, structural characterization, and the electronic properties of the oxidized A_2B electrenes. First, we have considered the one-sided full oxidized single layer electrene [O/A_2B], and in the sequence the two-sided full oxidized bilayer electrene [O/(A_2B)$_2$/O]. In Figs. 2(b1) and 2(b2) we present the structural models of O/A_2B and O/(A_2B)$_2$/O.

1. Energetic stability

The energetic stability of the oxidized electrenes was inferred through the calculation of the formation energy (E^f),

$$E^f = E[\text{O}_n/A_2B] - E[A_2B] - 2n\,E[\text{O}_2].$$

E[O$_n$/A_2B] and $E[A_2B]$ are the total energies of the oxidized and pristine A_2B electrenes, where n is the fraction of O adatoms per 2×2 surface unit cell, as shown Figs. 2(a1)–2(a3). The total energy calculations were performed by considering the full relaxation of the atomic positions, and the lattice vectors a and b in Fig. 2; $E[\text{O}_2]$ is the total energy of an isolated O_2 molecule (triplet state).

We found an energetic preference for oxygen adatoms on the hollow site aligned with the (cation) A atom at the opposite side of the A_2B monolayer, as shown in Figs. 2(a1)–2(a3) and 2(b1) for $n = 0.25, 0.50, 0.75$, and 1, respectively [33,68]. In Table IV (Appendix) we present a summary of our total energy results for oxygen adsorption on the other surface sites, namely aligned with the (cation) B atom, and on top of the A atom of the same surface side. Our formation energy results indicate that the oxidation processes are exothermic, with E^f (in absolute values) proportional to the oxidation rate. In Fig. 3(a) we present E^f as a function of the oxygen coverage for O/A_2B with B = N, O/A_2N. It is worth pointing out that, although the anionic electrons of A_2B are neutralized for coverage of 50% ($O_{0.5}/A_2B$), the incorporation of oxygen adatoms for $n > 50\%$ is energetically favorable. For instance, $O_{0.5}/Ca_2N$ plus an excess of O_2 molecules is less stable than the full oxidized O/Ca_2N system by 0.96 eV/O atom, $O_{0.5}/Ca_2N + O_2 \xrightarrow{-0.96} O/Ca_2N$. Similar results were obtained for the other O/A_2B systems. The formation energies

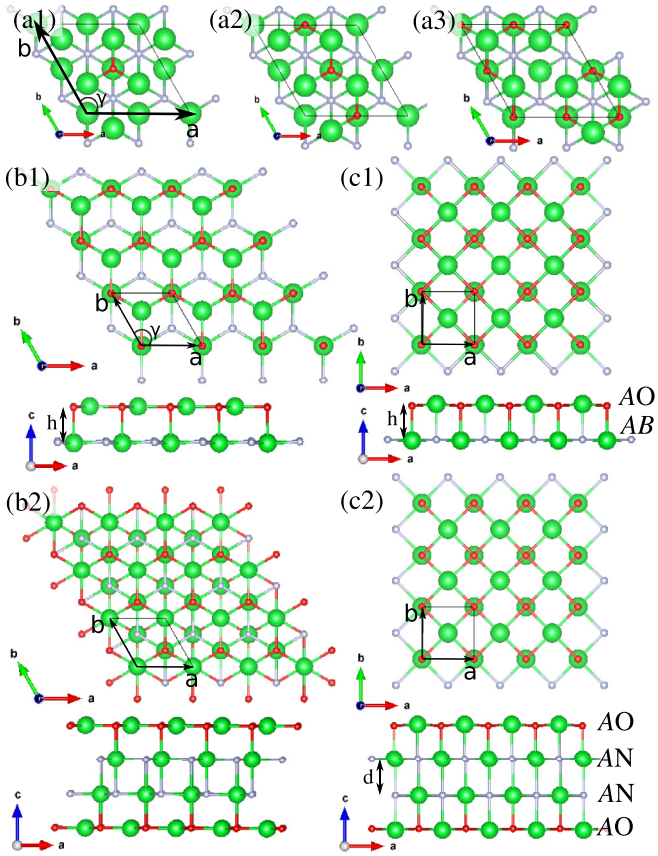

FIG. 2. Structural models of the hexagonal electrene adsorbed by O adatoms, with oxygen coverage (n) of 0.25 (a1), 0.50 (a2), and 0.75 (a3). Hexagonal (b1) and tetragonal (c1) one-sided full oxidized single layer electrene; two-sided full oxidized (b2) hexagonal and (c2) tetragonal bilayer electrene. Oxygen atoms are indicated by red spheres.

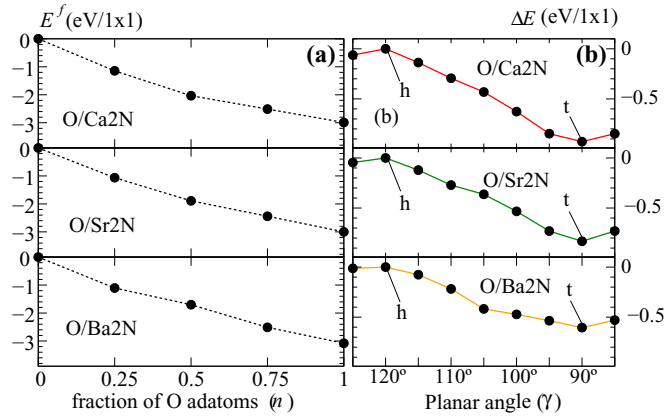

FIG. 3. (a) Formation energy of the oxidized O/A_2B electrene, and (b) the total energy difference as a function of the in-plane angle (γ) formed by the lattice vectors a and b [Fig. 2(b1)] of the fully oxidized electrenes O/A_2B, with $\gamma = 120^\circ$ for the hexagonal (h) phase and 90° for the tetragonal (t) phase.

and the equilibrium lattice constant of O/A_2B are summarized in Table II.

However, although the negative values of E^f, phonon spectra calculations (Fig. 4) revealed imaginary frequencies for all hexagonal O/A_2B structures [hereinafter referred to as O/$(A_2B)^{\rm h}$], except O/$(Y_2C)^{\rm h}$ [Fig. 4(d1)], thus indicating that the other O/$(A_2B)^{\rm h}$ systems are dynamically unstable. We have also examined structural stability of the hexagonal phases through molecular dynamics (MD) simulations, where found that all O/$(A_2B)^{\rm h}$ systems, with an exception for O/$(Y_2C)^{\rm h}$, are structurally unstable (Fig. 11, Appendix).

In the sequence we performed a search for dynamically and structurally stable O/A_2B by changing the in-plane angle (γ) formed by the lattice vectors a and b [Figs. 2(b1)]. Such a structural search was guided by the existence of stoichiometrically equivalent AO and AN tetragonal (t) bulk cubic parents, namely CaO, SrO, and BaO [69–72], and CaN, SrN, and BaN [72]. Our findings, for B = N, show that indeed the full oxidized hexagonal geometry [Fig. 2(b1)], $\gamma = 120^\circ$, corresponds to a metastable configuration characterized by a barrierless (h→t) structural transition [Fig. 3(b)] to a tetragonal ($\gamma = 90^\circ$) AO/AN layered phase $(AOAN)^{\rm t}$ [Fig. 2(c1)].

The energy gain upon such a h→t transition is given by the total energy difference between the two structural phases, $\Delta E^{\rm t\text{-}h} = E^{\rm t} - E^{\rm h}$. Our results of $\Delta E^{\rm t\text{-}h}$, presented in Table II, indicate that the tetragonal phase $(AOAB)^{\rm t}$ is energetically more favorable for all O/A_2B systems. On the other hand, phonon spectra calculations revealed that the $(AOAB)^{\rm t}$ systems are dynamically stable only for B = N $[(AOAN)^{\rm t}]$ and $(YOYC)^{\rm t}$. As shown in Fig. 4, imaginary frequencies present in the hexagonal O/A_2N structures [Figs. 4(a1)–4(c1)] were suppressed in the tetragonal $(CaOCaN)^{\rm t}$, $(SrOSrN)^{\rm t}$, and $(BaOBaN)^{\rm t}$ systems, Figs. 4(a2)–4(c2). In addition, the structural stability of $(AOAN)^{\rm t}$ and $(YOYC)^{\rm t}$ was confirmed by MD simulations. We found that the tetragonal structure was preserved at a temperature of 300 K during the 15 ps of MD simulation [Fig. 11 (Appendix)].

TABLE II. Formation energy (E^f in eV/1 × 1), for $n = 1$, of the hexagonal and tetragonal oxidized single layer (O/A_2B) and bilayer [O/$(A_2B)_2$/O] electrenes, and the total energy gain upon hexagonal→tetragonal structural transition ($\Delta E^{\rm h\text{-}t}$ in eV/O atom). The lattice constant (a) and the vertical distances (d and h in Fig. 2) are in Å. The lattice constant of the pristine hexagonal A_2B electrene are within parentheses.

O/A_2B	Hexagonal		⟶	Tetragonal	
A_2B	E^f	a	$\Delta E^{\rm h\text{-}t}$	a	h
Ca_2N	−2.99	3.85 (3.61)	−0.90	3.36	2.40
Sr_2N	−3.00	4.11 (3.85)	−0.80	3.59	2.54
Ba_2N	−3.08	4.35 (4.00)	−0.57	3.83	2.61
Y_2C	−5.46	3.64 (3.50)	−0.20	3.40	2.58
Ba_2As	−1.79	4.07 (4.65)	−0.51	3.75	2.80
Ba_2P	−2.08	4.42 (4.64)	−0.63	4.18	2.64
Sr_2P	−2.21	4.33 (4.43)	−0.76	3.92	2.50
O/$(A_2B)_2$/O	Hexagonal		⟶	Tetragonal	
A_2B	E^f	a	$\Delta E^{\rm h\text{-}t}$	a	d
Ca_2N	−3.04	3.92	−1.68	3.40	2.57
Sr_2N	−3.07	4.19	−1.27	3.63	2.85
Ba_2N	−3.02	4.33	−1.10	3.86	3.22

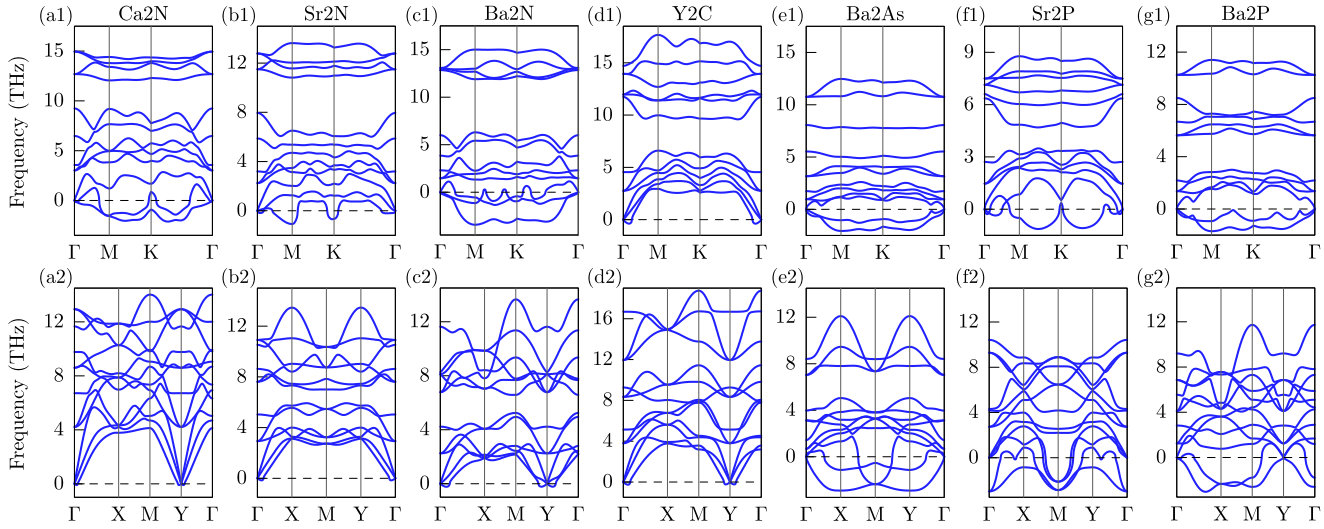

FIG. 4. Phonon spectra of the hexagonal (a1)–(g1) and tetragonal (a2)–(g2) O/A_2B electrenes.

We next have examined the surface oxidation of bilayer electrenes $[(A_2B)_2]$ with B = N, O/$(A_2\mathrm{N})_2$/O [Fig. 2(b2)]. Similarly to what we have found in the single layer systems, the O/$(A_2\mathrm{N})_2$/O structures are (i) energetically stable ($E^f < 0$ in Table II), and also (ii) present exothermic h→t structural transitions, with $\Delta E^{\text{t-h}}$ almost twice compared with those of their O/A_2B counterparts. Further phonon spectra calculations, and molecular dynamics simulations of O/$(A_2\mathrm{N})_2$/O, Figs. 5 and 12 (Appendix), respectively, show that the tetragonal (layered) systems, depicted in Fig. 2(c2), are dynamically and structurally stable. We found no imaginary frequencies in the tetragonal phases, Figs. 5(a2)–5(c2), and the MD simulations reveal that the atomic structures of the $(A\mathrm{O}(A\mathrm{N})_2A\mathrm{O})^{\text{t}}$ systems have been preserved [Figs. 12(a2)–12(c2), Appendix], whereas the ones of the hexagonal phase are no longer maintained after 15 ps of simulation, Figs. 12(a1)–12(c1) (Appendix).

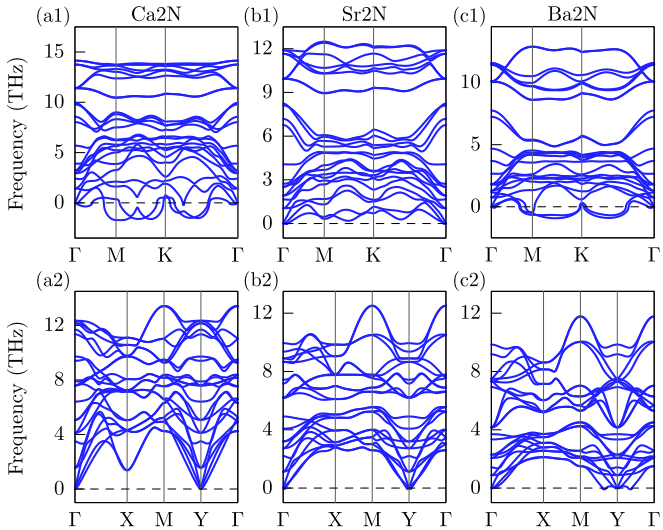

FIG. 5. Phonon spectra of the hexagonal (a1)–(c1), and tetragonal (a2)–(c2) O/$(A_2\mathrm{N})_2$/O electrenes.

At the equilibrium geometry, the tetragonal phase of the oxidized electrenes is characterized by a layered structure indicated as AO and AN in Fig. 2(c2), where the inner AN bilayer structure, with interlayer bond distance d (indicated in Table II), is shielded by oxidized AO sheets, $(A\mathrm{O}(A\mathrm{N})_2A\mathrm{O})^{\text{t}}$. As expected, such geometries somewhat mimic the ones of their (stoichiometrically equivalent and energetically stable) AO and AN bulk cubic parents, namely CaO, SrO, and BaO [69–72], and CaN, SrN, and BaN [72], thus providing further support to the energetic and structural stability of the tetragonal $(A\mathrm{O}(A\mathrm{N})_2A\mathrm{O})^{\text{t}}$.

2. *Structural characterization*

In order to present a more complete structural picture of the oxidized systems, in connection with their electronic properties, and also provide a theoretical support for future experimental studies, we have simulated the nitrogen K-edge x-ray absorption spectra of pristine (A_2N), and the oxidized O/A_2N and O/$(A_2\mathrm{N})_2$/O systems. Here we will present our results for A = Ca, namely Ca_2N, O/Ca_2N, and O/$(Ca_2N)_2$/O; the other systems, with A = Sr and Ba, present quite similar spectra and interpretations.

Let us start with the single layer pristine Ca_2N electrene. In Figs. 6(a1) and 6(b1) we present the absorption spectra for polarization vector perpendicular ($\hat{\varepsilon}^{\perp}$) and parallel ($\hat{\varepsilon}^{\parallel}$) to the surface, respectively. Based on the analysis of orbital projected density of states (DOS, not shown), we found that the edge and near-edge absorption features are mostly dictated by the electronic transition from the N-1s core electron to the unoccupied N-2p_z and N-2$p_{x,y}$ orbitals, for $\hat{\varepsilon}^{\perp}$ and $\hat{\varepsilon}^{\parallel}$, respectively. Due to the electronic confinement along the normal direction with respect to the electrene surface, the broadening of the absorption lines from the Fermi energy (E_{F}) up to $\sim E_{\text{F}} + 6$ eV for $\hat{\varepsilon}^{\perp}$ is slightly smaller compared with that for $\hat{\varepsilon}^{\parallel}$. Meanwhile, in the oxidized systems the energy broadenings for $\hat{\varepsilon}_{\parallel}$ [Figs. 6(d1) and 6(f1)] are significantly larger compared with those for $\hat{\varepsilon}_{\perp}$, Figs. 6(c1)–6(e1), indicating a reduction (increase) of the electronic confinement

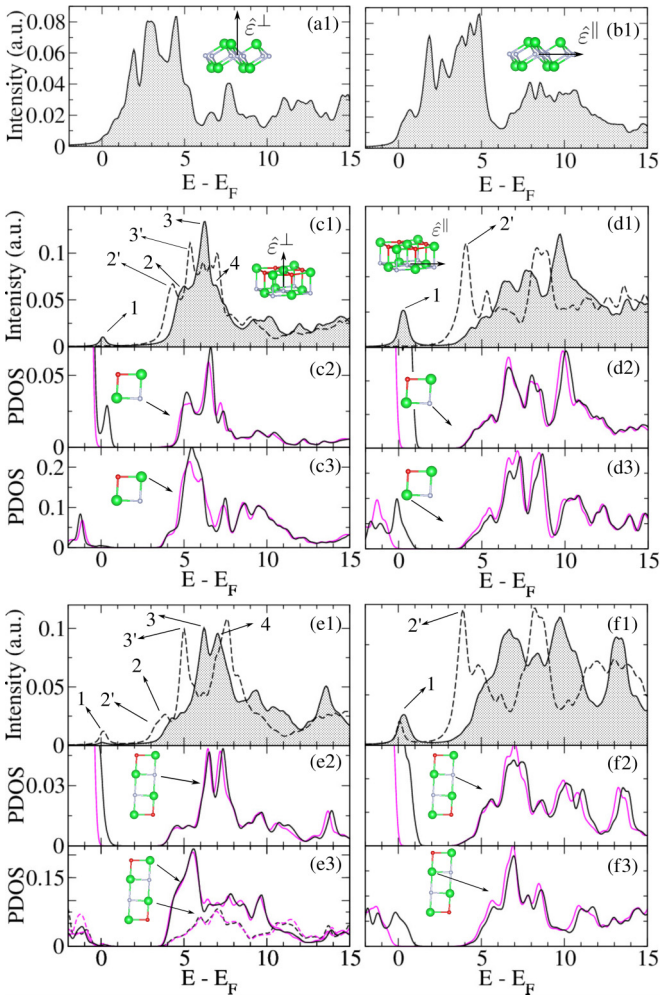

FIG. 6. XANES spectra of pristine single layer Ca_2N electrene for the polarization vector (a1) perpendicular, $\hat{\varepsilon}^{\perp}$, and (b1) parallel, $\hat{\varepsilon}^{\parallel}$, to the electrene surface. XANES spectra of O/Ca_2N for $\hat{\varepsilon}^{\perp}$ (c1), $\hat{\varepsilon}^{\parallel}$ (d1), and the density of states of $(CaOCaN)^t$ projected on the N-$2p_z$ (c2), Ca-$4p_z$ (c3), N-$2p_{x,y}$ (d2), and Ca-$4p_{x,y}$ (d3) orbitals. XANES spectra of O/$(Ca_2N)_2$/O, for $\hat{\varepsilon}^{\perp}$ (e1), $\hat{\varepsilon}^{\parallel}$ (f1), and the density of states of $(CaO(CaN)_2CaO)^t$ projected on the N-$2p_z$ (e2), Ca-$4p_z$ (e3), N-$2p_{x,y}$ (f2), and Ca-$4p_{x,y}$ (f3) orbitals. The XANES spectra of the tetragonal (hexagonal) phase are indicated by solid (dashed) lines. Spin-down and spin-up channels are indicated by purple and black solid lines.

along the parallel (perpendicular) direction with respect to the surface plane; which is, in its essence, a consequence of the formation of planar Ca–N and Ca–O layered structures upon oxidation [Fig. 2 and insets of Figs. 6(c1) and 6(d1)]. Further identification of the oxidized structures can be done by comparing the energy position of the absorption edges (AEs). For instance, comparing the AEs of the tetragonal phases, indicated by solid lines in Figs. 6(a1) and 6(c1), we find that the former lies near the Fermi level, while in the latter the AE starts at about $E_F + 4$ eV, thus indicating an increase of the N-1s binding energy (BE) in the oxidized systems. Indeed, based on the Löwdin charge population analysis, we found that the total charge of the nitrogen atoms in the oxidized O/Ca_2N [O/$(Ca_2N)_2$/O] electrenes reduces by 0.34 [0.42]e/N atom when compared with the one of pristine Ca_2N. Thus, we can infer that the increase of the N-1s BE is due to the reduction of the electronic screening at the N nucleus in the oxidized Ca_2N.

Next, we examine the nitrogen K-edge XANES spectra of the oxidized tetragonal systems in light of the projected density of states. The projections on the N-$2p_z$ and Ca-$4p_z$ orbitals, Figs. 6(c2) and 6(c3), indicate that the absorption features 2, 3, and 4 in Fig. 6(c1) are ruled by the electronic transitions to the lowest unoccupied N-$2p_z$ (major contribution) hybridized with the nearest neighbor Ca-$4p_z$ orbitals (minor contribution). It is worth noting that the features 2 and 3 (for $\hat{\varepsilon}^{\perp}$) of the tetragonal phase are also present in the absorption spectra of the hexagonal phase [2′ and 3′ (dashed lines) in Fig. 6(c1)]. However they are shifted by ∼1 eV toward lower energies when compared with their counterparts 2 and 3, thus we can infer that the BE of the N-1s core electrons in the tetragonal phase is larger compared with the one of the hexagonal phase. As discussed above, such an increase of the BE is supported by the reduction of the total charge of the nitrogen atoms (by 0.01e/N atom) in the tetragonal O/Ca_2N in comparison with that of hexagonal one. Similarly for O/$(Ca_2N)_2$/O, as shown Figs. 6(e1)–6(e3), (i) the XANES spectra ($\hat{\varepsilon}^{\perp}$) of the tetragonal phase is ruled by the unoccupied N-$2p_z$ states (major contribution) hybridized with the $4p_z$ orbitals (minor contribution) of the Ca atoms embedded in the CaO sheets; and (ii) the edge features of the tetragonal and hexagonal phases indicate that the BE of N-1s core electrons of the former is larger by about 1 eV compared with that of the latter, in agreement with the lower total charge (by 0.04e/N atom) of the N atoms in the tetragonal phase.

In Figs. 6(d) and 6(f) we present the XANES spectra for a polarization vector parallel to the O/Ca_2N and O/$(Ca_2N)_2$/O layers, $\hat{\varepsilon}^{\parallel}$, and the DOS projected on the N-$2p_{x,y}$ and Ca-$4p_{x,y}$ orbitals of the tetragonal phase. Compared with the absorption spectra with the polarization vector normal to the surface $\hat{\varepsilon}^{\perp}$, we found that the pre-edge absorption (feature 1), attributed to the hybridizations of the partially occupied spin-down N-$2p_{x,y}$ and Ca-$4p_{x,y}$ orbitals, becomes more intense for $\hat{\varepsilon}^{\parallel}$. In fact, such a pre-edge absorption spectrum can be considered as a signature of the formation of half-metallic channels along the CaN layers, which will be discussed below. In the sequence, it is noticeable the well defined absorption spectrum 2′, present in the hexagonal phase, has been practically suppressed in the tetragonal structure, thus suggesting that the structural differences between the tetragonal and hexagonal phases are better captured by looking at the in-plane edge absorption features.

3. Electronic and magnetic properties

The electronic band structures of A_2B electrenes, with A = Ca, Sr, Ba, and B = N are characterized by parabolic metallic bands, giving rise to nearly free electron (NFE) states localized on the electrene's surface and between the stacked layers. On the other hand, upon the formation of AO oxidized layers these NFE states become unoccupied, and we observe the emergence of magnetic moments in the AN layers. Here we will examine the magnetic and electronic properties of $(AOAN)^t$ and $(AO(AN)_2AO)^t$.

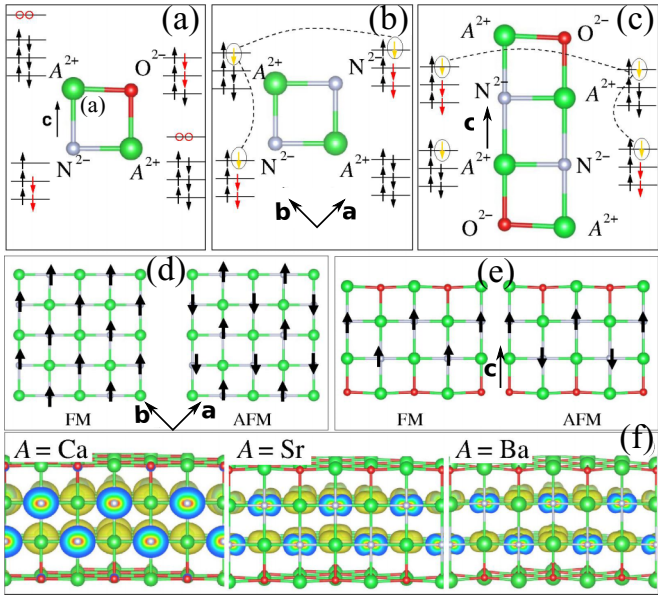

FIG. 7. Schematic orbital occupation of $(AOAN)^t$ (a) AO and NO layers along the stacking direction (c), and (b) AN sheet perpendicular to the stacking direction, a × b plane. (c) Orbital occupation of $(AO(AN)_2AO)^t$ along the stacking direction. (d) Intralayer and (e) interlayer FM/AFM spin polarizations. (f) Spin-density distribution of the (intralayer and interlayer) FM $(AO(AN)_2AO)^t$ systems. Isosurface of $0.004e/\text{Å}^2$.

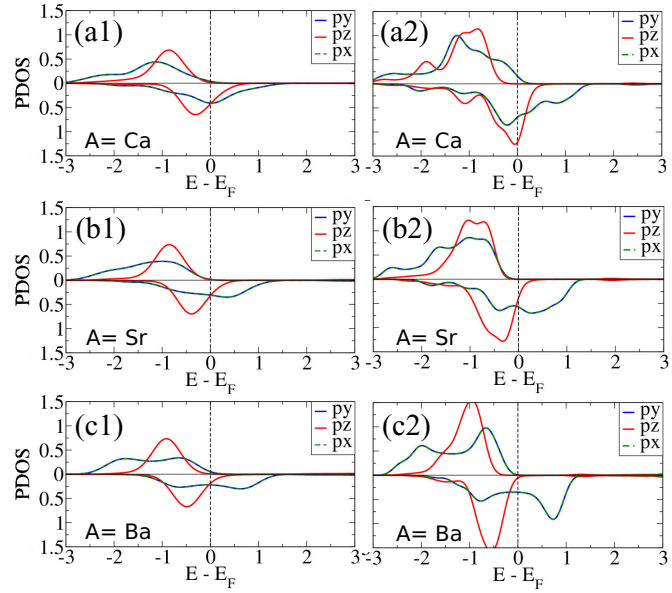

FIG. 8. Electronic density of states (DOS) projected on the N-2p orbitals of $(AOAN)^t$ (a1)–(c1), and $(AO(AN)_2AO)^t$ (a2)–(c2).

Based on the nominal oxidation states and the electronegativities of the involved atoms, we can infer the emergence of a magnetic moment in the oxidized systems [32]. There is a net charge transfer of two electrons from each (less electronegative) A atoms to the (more electronegative) O and N atoms, resulting in A^{2+}, O^{2-}, and N^{2-} oxidation states, Fig. 7(a). The ground state configuration is characterized by an OA (oxidized) layer with closed p shells parallel to a AN layer with the N-2p orbitals partially occupied, Fig. 7(b). Similarly, in the bilayer system $(AO(AN)_2AO)^t$ [Fig. 7(c)], we find AN layers with partially occupied N-2p orbitals sandwiched by OA (edge) layers with closed p shells. According to the Hund's rule, each N atom will carry a net magnetic moment of 1 μ_B. Indeed, within the GGA-PBE approach, we found a net magnetic moment of about 0.8 μ_B mostly localized on the nitrogen atoms [44]. The projected electronic density of states (PDOS) on the N-2p orbitals of $(AOAN)^t$ and $(AO(AN)_2AO)^t$, Figs. 8(a)–8(c), reveal that the partial occupation of planar N-$2p_{x,y}$ orbitals brings the major contribution to the polarization of the N atoms.

Total energy comparisons between the magnetic and nonmagnetic phases, $\Delta E^{\text{mag}} = E^{\text{mag}} - E^{\text{nonmag}}$, support the energetic preference for the spin-polarized systems, $\Delta E^{\text{mag}} < 0$ in Table III. The strength of the magnetic interactions between the nitrogen atoms was examined by comparing the total energies of the ferromagnetic (FM) and antiferromagnetic (AFM) phases for the intralayer ($\Delta E^{\text{FM-AFM}}_{\text{intra}}$) and interlayer ($\Delta E^{\text{FM-AFM}}_{\text{inter}}$) magnetic couplings, as shown in Figs. 7(d) and 7(e), respectively. The intralayer coupling takes place between the N atoms in the same AN layer [Fig. 7(d)], while the interlayer coupling is due to the interactions between the N atoms lying in different AN layers of $(AO(AN)_2AO)^t$, Fig. 7(e). Our results, summarized in Table III, reveal that both systems, $(AOAN)^t$ and $(AO(AN)_2AO)^t$, present an energetic preference for the intralayer and interlayer FM coupling between the N atoms. It is noticeable that (i) $(CaO(CaN)_2CaO)^t$ presents the largest interlayer FM interaction, $\Delta E^{\text{FM-AFM}}_{\text{inter}} = -36.5$ meV/N atom, when compared with the other $(AO(AN)_2AO)^t$ systems, leading to (ii) a strengthening of the intralayer FM coupling, namely $\Delta E^{\text{FM-AFM}}_{\text{intra}} = -8.5 \rightarrow -22.8$ meV/N atom. In contrast, (iii) we found (relatively) lower values of $\Delta E^{\text{FM-AFM}}_{\text{inter}}$ for $(SrO(SrN)_2SrO)^t$ and $(BaO(BaN)_2BaO)^t$ which can be due to the larger interlayer distance (d) as indicated in Fig. 2(c2) and Table II, and the more localized feature of the spin-polarized states normal to the stacking direction (c). In Fig. 7(f) we present the spin-density distribution of the intralayer and interlayer FM $(AO(AN)_2AO)^t$, with A = Ca, Sr, and Ba where we confirm the localization of the net magnetic moment on the nitrogen atoms. It is noticeable that the projection of the DOS on the N-2p orbitals (Fig. 8) support the larger interlayer interaction ruled by the N-2p_z orbitals in $(CaO(CaN)_2CaO)^t$

TABLE III. Total energy differences (in meV/N atom) between nonmagnetic and magnetic phases, $\Delta E^{\text{mag}} = E^{\text{mag}} - E^{\text{nonmag}}$, and between the FM and AFM phases for intralayer ($\Delta E^{\text{FM-AFM}}_{\text{intra}}$), and interlayer ($\Delta E^{\text{FM-AFM}}_{\text{inter}}$) interactions, schematically shown in Figs. 7(d) and 7(e), respectively.

	ΔE^{mag}	$\Delta E^{\text{FM-AFM}}_{\text{intra}}$	$\Delta E^{\text{FM-AFM}}_{\text{inter}}$
$(CaOCaN)^t$	−67	−8.5	–
$(SrOSrN)^t$	−135	−18.7	–
$(BaOBaN)^t$	−92	−1.9	–
$(CaO(CaN)_2CaO)^t$	−83	−22.8	−36.5
$(SrO(SrN)_2SrO)^t$	−127	−12.9	−1.0
$(BaO(BaN)_2BaO)^t$	−93	−4.4	−0.5

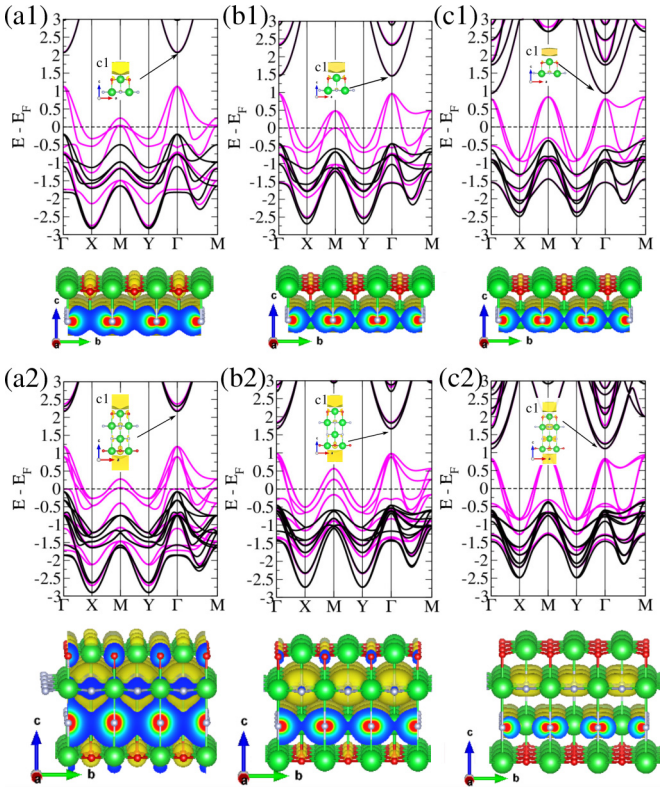

FIG. 9. Electronic band structure of the electronic distribution near the Fermi level ($E_F \pm 0.1$ eV) of the oxidized $(AOAB)^t$ monolayer with A = Ca (a1), Sr (b1), and Ba (c1), and the oxidized $(AO(AB)_2AO)^t$ bilayer with A = Ca (a2), Sr (b2), and Ba (c2). Electronic distribution of the NFE state at the Γ point (inset). Isosurfaces of $0.002e/Å^2$. Solid purple and black lines indicate the spin-down and spin-up channels.

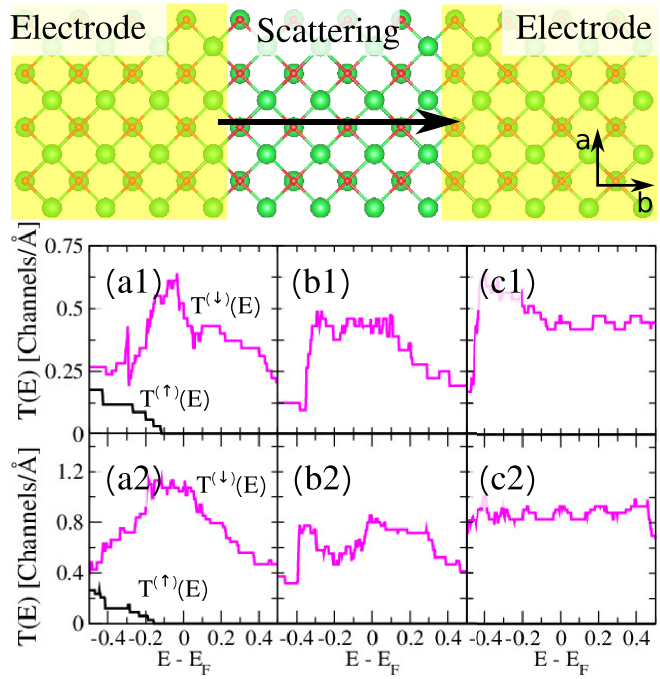

FIG. 10. (Top) Structural model of the simulation setup used for the electronic transport calculation along the b direction. Transmission probability and electronic current of the $(AOAB)^t$ oxidized electrene with A = Ca (a1), Sr (b1), and Ba (c1), and $(AO(AB)_2AO)^t$ with A = Ca (a2), Sr (b2), and Ba (c2).

[Fig. 8(a2)] compared with those of the other oxidized bilayer electrenes, Figs. 8(b2) and 8(c2).

The energetic preference for the FM phase can be attributed to superexchange interactions between the N^{2-} anions mediated by A^{2+} cations. In this sense, the FM coupling will be favored due to the electron delocalization along the N^{2-}–A^{2+}–N^{2-} bonds, thus lowering the kinetic energy of the system, as schematically shown in Figs. 7(b) and 7(c) for the intralayer and interlayer couplings, respectively. Further support to the FM coupling between the N^{2-} anions, mediated by superexchange interactions, can be found in the Goodenough-Kanamori rule [73,74], since the N^{2-}–A^{2+}–N^{2-} bonds are characterized by bond angles of 90°.

The electronic band structures of $(AOAN)^t$ and $(AO(AN)_2AO)^t$, Fig. 9, indicate they are half-metals. The metallic channels are characterized by spin-down (purple lines), whereas the spin-up energy bands (black lines) are a semiconductor with the valence band maximum (VBM) lying at about 0.2 eV below the Fermi level ($E^{VBM} \approx E_F - 0.2$ eV) for A = Ca [Figs. 9(a1) and 9(a2)] while for A = Sr and Ba we find $E^{VBM} \approx E_F - 0.5$ eV, Figs. 9(b1) and 9(b2) and 9(c1) and 9(c2). The lowest unoccupied states are spin degenerated, lying between 1 and 2 eV above E_F, and characterized by NFE parabolic bands localized on the oxidized surface (OA) (insets of Fig. 9). Further real space projections of the electronic states near the Fermi level $E_F \pm 0.1$ eV reveal that the half-metallic bands are mostly ruled by in-plane N-2p orbitals localized in the AN layers of $(AOAN)^t$, Figs. 9(a1)–9(c1). Similarly, in the bilayer systems the half-metallic bands spread out through the AN layers; however, it is worth noting that in $(AO(AN)_2AO)^t$, these half-metallic channels are sandwiched by the oxidized AO sheets [Figs. 9(a2)–9(c2)]. These oxidized sheets may act as a shield, protecting the half-metallic channels against the environment conditions, which is a quite appealing property for development of spintronic devices based on 2D platforms.

TABLE IV. Total energy differences (in eV/O atom) between the (energetically most stable) O adatom on the hollow site aligned with the A atom at the opposite surface side of the A_2B monolayer [E(i)], and the O adatom on the hollow site aligned with the B atom [E(ii)], and the O adatom on the on-top site aligned with A atom of the same surface side, $\Delta E(\text{ii}) = E(\text{i}) - E(\text{ii})$ and $\Delta E(\text{iii}) = E(\text{i}) - E(\text{iii})$, respectively.

O/A_2B	ΔE(ii)	ΔE(iii)
O/Ca_2N	−0.12	−2.82
O/Sr_2N	−0.19	−2.77
O/Ba_2N	−0.34	−2.60
O/Y_2C	−0.33	−2.91
O/Ba_2As	−0.12	−2.82
O/Sr_2P	−0.15	−3.37
O/Ba_2P	−0.19	−2.75

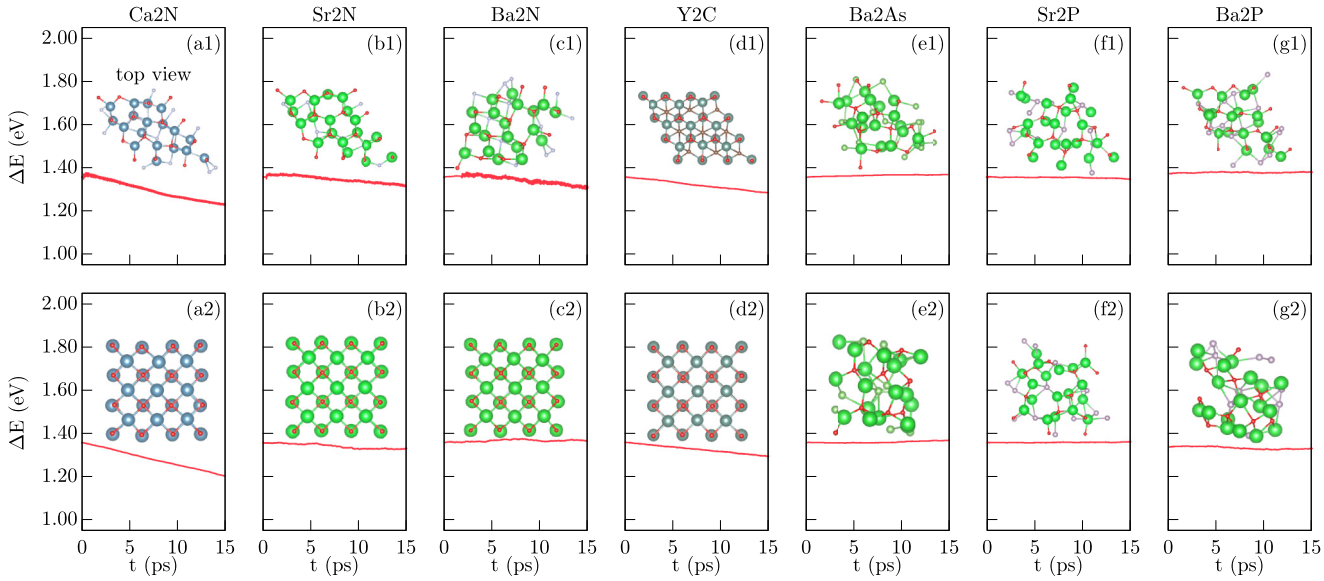

FIG. 11. Total energy fluctuation, of hexagonal (a1)–(g1) and tetragonal (a2)–(g2) O/A_2B oxidized electrenes, as a function of the time step (1 fs). Insets, Structural model after 15 ps of molecular dynamics simulation at 300 K.

In order to provide a quantitative picture of the emergence of spin-polarized electronic current in the oxidized electrenes, we calculate the electronic transmission probability $T(E)$ and the electronic current $I(V)$ of the $(AOAN)^t$ and $(AO(AN)_2AO)^t$ systems. In Fig. 10 (top) we present the simulation setup used for the electronic transport calculations along the b direction, namely two (left and right) electrodes composed by semi-infinite oxidized electrenes, both connected to a (central) scattering region. Our results of $T(E)$, summarized in Figs. 10(a1)–10(a3) and 10(b1)–10(b3), reveal that near the Fermi level ($|E_F| \leqslant 0.1$ eV) the transmission probability is mediated by the spin-down channels, in consonance with the electronic band structure results (Fig. 9). The transmission channels lie on the inner AN layers, mostly ruled by the in-plane hybridizations between the spin-down N-2p orbitals (N-2$p^{(\downarrow)}_{x,y}$) with the nearest neighbor A atoms. For A = Ca we found larger values of $T(E)$ [Figs. 10(a1) and 10(a2)], and net electronic current [Figs. 13(a1) and 13(a2) in the Appendix] when compared with the other $(AOAN)^t$ and $(AO(AN)_2AO)^t$ systems. In contrast, although the more localized character of the in-plane N-2$p^{(\downarrow)}_{x,y}$ orbitals for A = Ba [Figs. 9(c1) and 9(c2)] compared with the ones obtained for A = Sr, Figs. 9(b1) and 9(b2), we found nearly the same values of transmission probability, Figs. 10(b1) and 10(b2) and 10(c1) and 10(c2), and electronic current for low bias voltage [Figs. 13(b1)–13(c1) and 13(c1) and 13(c2) in the Appendix]. We have also calculated the transmission probability and the electronic current along the bisector direction between a and b, where we found practically the same values of $T(E)$ and

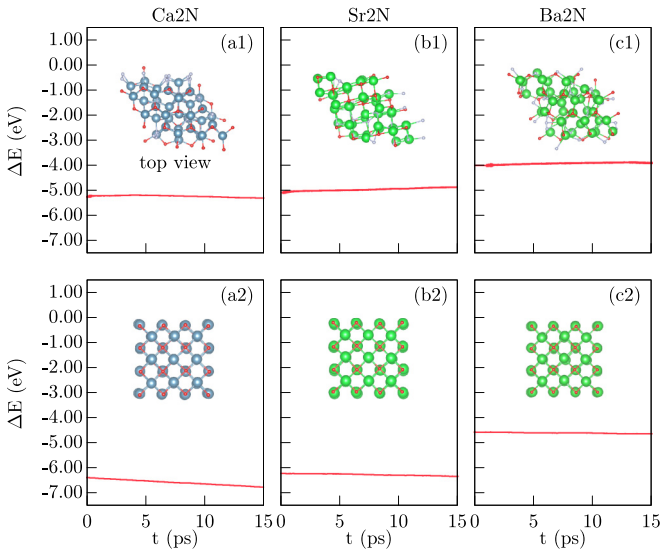

FIG. 12. Total energy fluctuation, of hexagonal (a1)–(c1), and tetragonal (a2)–(c2) O/$(A_2N)_2$/O oxidized electrenes, as a function of the time step (1 fs). Insets: Structural model after 15 ps of molecular dynamics simulation at 300 K.

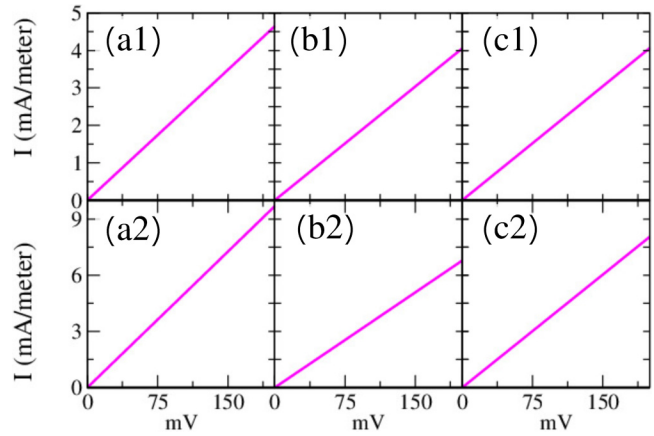

FIG. 13. Electronic current of $(AOAB)^t$ with A = Ca (a1), Sr (b1), and Ba (c1), and $(AO(AB)_2AO)^t$ with A = Ca (a2), Sr (b2), and Ba (c2).

$I(V)$ near the Fermi level. Thus, suggesting that the electronic transport through the inner AN layers, at low bias limit, does not present significant directional anisotropy as predicted in the other 2D systems [75].

IV. SUMMARY AND CONCLUSIONS

By means of first-principles DFT calculations, we have performed a theoretical study of the full oxidized 2D single layer, O/A_2B, and bilayer, O/$(A_2B)_2$/O, electrenes, with A = Ba, Ca, Sr, Y, and B = As, N, P, C. We found that O/A_2B and O/$(A_2B)_2$/O systems with A = Ca, Sr, Ba, and B = N become stable upon an hexagonal→tetragonal structural transition, resulting in layered tetragonal systems, $(AOAN)^t$ and $(AO(AN)_2AO)^t$. Further characterizations, through simulations of XANES spectroscopy, allowed us to identify key aspects of the absorption spectra and their correlation with the structural and electronic properties of the oxidized systems. We found the emergence of a ferromagnetic phase in the oxidized tetragonal structures, with the net magnetic moment mostly ruled by the planar N-2$p_{x,y}$ orbitals. Meanwhile, electronic structure calculations reveal the formation of half-metallic bands spreading out through the AN layers, with nearly negligible contribution from the oxidized AO sheets. The emergence of spin-polarized transmission channels was confirmed through the electronic transport calculations based on the Landauer-Büttiker formalism. These results reveal that the oxidized $(AOAN)^t$ and $(AO(AN)_2AO)^t$ systems are quite interesting platforms for spin-polarized transport on 2D systems, characterized spin-polarized metallic channels shielded by oxide layers. For instance, $(AO(AN)_2AO)^t$ can be viewed as a core-shell 2D material with half-metallic channels lying on the $(AN)_2$ layers (core) protected against the environment conditions by the oxidized AO sheets (shell).

ACKNOWLEDGMENTS

The authors acknowledge financial support from the Brazilian agencies CNPq, CAPES, FAPEMIG, and INCT-Nanomateriais de Carbono, and the CENAPAD-SP and Laboratório Nacional de Computação Científica (LNCC-SCAFMat2) for computer time.

APPENDIX

In Table IV we present the total energy differences between the O/A_2B electrenes with the oxygen atom adsorbed on the (i) hollow site aligned with the cation A atom at the opposite surface side of the A_2B monolayer, (ii) on the hollow site aligned with the B atom, and (iii) on top of the A atom of the same surface side, namely $\Delta E(\text{ii}) = E(\text{i}) - E(\text{ii})$, and $\Delta E(\text{iii}) = E(\text{i}) - E(\text{iii})$, respectively. Our results of ΔE, viz. $\Delta E(\text{ii}) < 0$ and $\Delta E(\text{iii}) < 0$, confirm the energetic preference of (i). In Figs. 11 and 12 we present our results of MD simulation to oxidized single layer electrene, O/A_2B, with A = Ca, Sr, Ba, Y, and B = N, P, As, C, and bilayer (O/$(A_2N)_2$/O) electrenes, with A = Ca, Sr, and Ba. We have considered a total simulation time of 15 ps, and time steps of 1 fs. In the inset we present the structural model after 15 ps of simulation at 300 K.

In Fig. 13 we present the net electronic current of the oxidized monolayer $(AOAB)^t$ and bilayer $(AO(AB)_2AO)^t$ systems by using Landauer-Büttiker formula as described in Sec. II.

[1] K. S. Novoselov, A. K. Geim, S. V. Morozov, D. Jiang, Y. Zhang, S. V. Dubonos, I. V. Grigorieva, and A. A. Firsov, Science **306**, 666 (2004).
[2] C. L. Kane and E. J. Mele, Phys. Rev. Lett. **95**, 146802 (2005).
[3] C. Weeks, J. Hu, J. Alicea, M. Franz, and R. Wu, Phys. Rev. X **1**, 021001 (2011).
[4] C. M. Acosta, M. P. Lima, R. H. Miwa, A. J. R. da Silva, and A. Fazzio, Phys. Rev. B **89**, 155438 (2014).
[5] T. Song, Z. Fei, M. Yankowitz, Z. Lin, Q. Jiang, K. Hwangbo, Q. Zhang, B. Sun, T. Taniguchi, K. Watanabe *et al.*, Nat. Mater. **18**, 1298 (2019).
[6] T. Li, S. Jiang, N. Sivadas, Z. Wang, Y. Xu, D. Weber, J. E. Goldberger, K. Watanabe, T. Taniguchi, C. J. Fennie *et al.*, Nat. Mater. **18**, 1303 (2019).
[7] E. S. Morell, A. León, R. H. Miwa, and P. Vargas, 2D Mater. **6**, 025020 (2019).
[8] D. P. de A. Deus, I. S. S. de Oliveira, J. B. Oliveira, W. L. Scopel, and R. H. Miwa, Phys. Rev. Materials **5**, 054002 (2021).
[9] B. Radisavljevic, A. Radenovic, J. Brivio, i. V. Giacometti, and A. Kis, Nat. Nanotechnol. **6**, 147 (2011).
[10] Y. Tong, Y. Guo, K. Mu, H. Shan, J. Dai, Y. Liu, Z. Sun, A. Zhao, X. C. Zeng, C. Wu *et al.*, Adv. Mater. **29**, 1703123 (2017).
[11] V. V. Kulish and W. Huang, J. Mater. Chem. C **5**, 8734 (2017).
[12] G. Gökoğlu and E. Aktürk, Mater. Res. Express **4**, 116305 (2017).
[13] Y. Feng, X. Wu, J. Han, and G. Gao, J. Mater. Chem. C **6**, 4087 (2018).
[14] B. Wang, Q. Wu, Y. Zhang, Y. Guo, X. Zhang, Q. Zhou, S. Dong, and J. Wang, Nanoscale Horizons **3**, 551 (2018).
[15] D. L. Druffel, A. H. Woomer, K. L. Kuntz, J. T. Pawlik, and S. C. Warren, J. Mater. Chem. C **5**, 11196 (2017).
[16] S. Liu, W. Li, S. W. Kim, and J.-H. Choi, J. Phys. Chem. C **124**, 1398 (2020).
[17] K. Lee, S. W. Kim, Y. Toda, S. Matsuishi, and H. Hosono, Nature (London) **494**, 336 (2013).
[18] J. S. Oh, C.-J. Kang, Y. J. Kim, S. Sinn, M. Han, Y. J. Chang, B.-G. Park, S. W. Kim, B. I. Min, H.-D. Kim *et al.*, J. Am. Chem. Soc. **138**, 2496 (2016).
[19] N. E. Brese and M. O'Keeffe, J. Solid State Chem. **87**, 134 (1990).
[20] X. Zhang, Z. Xiao, H. Lei, Y. Toda, S. Matsuishi, T. Kamiya, S. Ueda, and H. Hosono, Chem. Mater. **26**, 6638 (2014).
[21] T. Tada, S. Takemoto, S. Matsuishi, and H. Hosono, Inorg. Chem. **53**, 10347 (2014).
[22] T. Inoshita, S. Jeong, N. Hamada, and H. Hosono, Phys. Rev. X **4**, 031023 (2014).
[23] Y. Zhang, H. Wang, Y. Wang, L. Zhang, and Y. Ma, Phys. Rev. X **7**, 011017 (2017).
[24] J. Zhou, L. Shen, M. Yang, H. Cheng, W. Kong, and Y. P. Feng, Chem. Mater. **31**, 1860 (2019).

[25] N. Mounet, M. Gibertini, P. Schwaller, D. Campi, A. Merkys, A. Marrazzo, T. Sohier, I. E. Castelli, A. Cepellotti, G. Pizzi *et al.*, Nat. Nanotechnol. **13**, 246 (2018).

[26] S. Zhao, Z. Li, and J. Yang, J. Am. Chem. Soc. **136**, 13313 (2014).

[27] D. L. Druffel, K. L. Kuntz, A. H. Woomer, F. M. Alcorn, J. Hu, C. L. Donley, and S. C. Warren, J. Am. Chem. Soc. **138**, 16089 (2016).

[28] X. Zeng, S. Zhao, Z. Li, and J. Yang, Phys. Rev. B **98**, 155443 (2018).

[29] S. Zhang, M. Kang, H. Huang, W. Jiang, X. Ni, L. Kang, S. Zhang, H. Xu, Z. Liu, and F. Liu, Phys. Rev. B **99**, 100404(R) (2019).

[30] L. Liu and H. L. Zhuang, Mater. Res. Express **5**, 076306 (2018).

[31] X.-L. Qiu, J.-F. Zhang, Z.-Y. Lu, and K. Liu, J. Phys. Chem. C **123**, 24698 (2019).

[32] C.-W. Wu and D.-X. Yao, J. Magn. Magn. Mater. **493**, 165727 (2020).

[33] P. H. Souza, J. E. Padilha, and R. H. Miwa, J. Phys. Chem. C **124**, 14706 (2020).

[34] P. Hohenberg and W. Kohn, Phys. Rev. **136**, B864 (1964).

[35] P. Giannozzi, S. Baroni, N. Bonini, M. Calandra, R. Car, C. Cavazzoni, D. Ceresoli, G. L. Chiarotti, M. Cococcioni, I. Dabo *et al.*, J. Phys.: Condens. Matter **21**, 395502 (2009).

[36] G. Kresse and J. Furthmüller, Comput. Mater. Sci. **6**, 15 (1996).

[37] G. Kresse and J. Furthmüller, Phys. Rev. B **54**, 11169 (1996).

[38] J. P. Perdew, K. Burke, and M. Ernzerhof, Phys. Rev. Lett. **77**, 3865 (1996).

[39] D. R. Hamann, Phys. Rev. B **88**, 085117 (2013).

[40] P. E. Blöchl, Phys. Rev. B **50**, 17953 (1994).

[41] L. Bengtsson, Phys. Rev. B **59**, 12301 (1999).

[42] W. Kohn and L. J. Sham, Phys. Rev. **140**, A1133 (1965).

[43] H. J. Monkhorst and J. D. Pack, Phys. Rev. B **13**, 5188 (1976).

[44] We have verified the accuracy of our total energy results by using the VASP code, by using $15 \times 15 \times 1$ special k points [43] to the Brillouin zone sampling, and energy cutoff of 600 eV for the plane wave basis set.

[45] M. Dion, H. Rydberg, E. Schröder, D. C. Langreth, and B. I. Lundqvist, Phys. Rev. Lett. **92**, 246401 (2004).

[46] G. Roman-Perez and J. M. Soler, Phys. Rev. Lett. **103**, 096102 (2009).

[47] J. Klimeš, D. R. Bowler, and A. Michaelides, Phys. Rev. B **83**, 195131 (2011).

[48] Oana Bunău and M. Calandra, Phys. Rev. B **87**, 205105 (2013).

[49] C. Gougoussis, M. Calandra, A. P. Seitsonen, and F. Mauri, Phys. Rev. B **80**, 075102 (2009).

[50] M. Taillefumier, D. Cabaret, A.-M. Flank, and F. Mauri, Phys. Rev. B **66**, 195107 (2002).

[51] C. J. Pickard and F. Mauri, Phys. Rev. B **63**, 245101 (2001).

[52] A. Dal Corso, Comput. Mater. Sci. **95**, 337 (2014).

[53] A. Togo and I. Tanaka, Scr. Mater. **108**, 1 (2015).

[54] S. Nosé, J. Chem. Phys. **81**, 511 (1984).

[55] J. M. Soler, E. Artacho, J. D. Gale, A. García, J. Junquera, P. Ordejón, and D. Sánchez-Portal, J. Phys.: Condens. Matter **14**, 2745 (2002).

[56] M. Brandbyge, J.-L. Mozos, P. Ordejón, J. Taylor, and K. Stokbro, Phys. Rev. B **65**, 165401 (2002).

[57] E. Artacho, D. Sánchez-Portal, P. Ordejón, A. Garcia, and J. M. Soler, Phys. Status Solidi B **215**, 809 (1999).

[58] Within the SIESTA code, the cutoff radius of the basis set (pseudoatomic orbitals) can be tuned by a single parameter, *energy shift*. For lower *energy shift* we have larger cutoff radii for the atomic orbitals, that is, the basis set has been improved. In the present work we have considered an energy shift of 0.10 eV to determine the radius cutoff of the pseudoatomic orbitals. Here we verify the convergence of our total energy results for an *energy shift* of 0.05 eV.

[59] M. Büttiker, Y. Imry, R. Landauer, and S. Pinhas, Phys. Rev. B **31**, 6207 (1985).

[60] R. Landauer, Y. Imry, M. Büttiker, and S. Pinhas, IBM J. Res. Dev. **32**, 306 (1988).

[61] W. Ming, M. Yoon, M.-H. Du, K. Lee, and S. W. Kim, J. Am. Chem. Soc. **138**, 15336 (2016).

[62] J. Hou, K. Tu, and Z. Chen, J. Phys. Chem. C **120**, 18473 (2016).

[63] D. H. Gregory, A. Bowman, C. F. Baker, and D. P. Weston, J. Mater. Chem. **10**, 1635 (2000).

[64] J. Wang, L. Li, Z. Shen, P. Guo, M. Li, B. Zhao, L. Fang, and L. Yang, Materials **11**, 2462 (2018).

[65] O. Reckeweg and F. DiSalvo, Z. Kristal.-New Cryst. Structures **220**, 519 (2005).

[66] J. H. Jung, C.-H. Park, and J. Ihm, Nano Lett. **18**, 2759 (2018).

[67] S. G. Dale and E. R. Johnson, Phys. Chem. Chem. Phys. **19**, 27343 (2017).

[68] W. Li, Y. You, and J.-H. Choi, J. Phys. Chem. C **124**, 25316 (2020).

[69] M. Dadsetani and R. Beiranvand, Solid State Sci. **11**, 2099 (2009).

[70] H. Nejatipour and M. Dadsetani, Phys. Scr. **90**, 085802 (2015).

[71] D. K. Nguyen, V. Van On, D. Hoat, J. Rivas-Silva, and G. H. Cocoletzi, Phys. Lett. A **397**, 127241 (2021).

[72] A. Jain, S. P. Ong, G. Hautier, W. Chen, W. D. Richards, S. Dacek, S. Cholia, D. Gunter, D. Skinner, G. Ceder, and K. a. Persson, APL Mater. **1**, 011002 (2013).

[73] J. B. Goodenough, Phys. Rev. **100**, 564 (1955).

[74] J. Kanamori, J. Appl. Phys. **31**, S14 (1960).

[75] J. E. Padilha, R. H. Miwa, and A. Fazzio, Phys. Chem. Chem. Phys. **18**, 25491 (2016).